

Electronic phase transition in the Re_3Ge_7 endohedral cluster compoundV. Yu. Verchenko ^{1,2,*}, M. S. Likhhanov ¹, A. V. Mironov,¹ and A. V. Shevelkov¹¹*Department of Chemistry, Lomonosov Moscow State University, 119991 Moscow, Russia*²*National Institute of Chemical Physics and Biophysics, 12618 Tallinn, Estonia*

(Received 25 July 2022; revised 6 October 2022; accepted 9 November 2022; published 18 November 2022)

Re_3Ge_7 is a unique electronic material showing low-temperature metal–insulator-like phase transition. Furthermore, bulk superconductivity can be induced in Re_3Ge_7 by hole doping. Here, we present transport properties, temperature-dependent high-resolution powder x-ray diffraction study, and electronic structure of Re_3Ge_7 in the vicinity of the electronic phase transition. Electrical resistivity and heat capacity measurements confirm the anomaly at 58.5 K in zero magnetic field. The Seebeck coefficient changes its sign and exhibits a maximum below the transition temperature indicating substantial changes in the electronic structure. Temperature-dependent structural studies confirm the second-order nature of phase transition, where unit cell parameters show abrupt change at the transition temperature. An analysis of interatomic distances indicates that the shrinkage of the unit cell volume is due to the interatomic changes taking place in the second coordination sphere of Re atoms. Electronic structure calculations reveal strong $5d - 4p$ hybridization of valence orbitals near the Fermi level, which is situated between two deep pseudogaps of the density of states. The transition to the semiconducting state is accompanied by the opening of a band gap at the Fermi level right above the narrow pocket of hybridized states.

DOI: [10.1103/PhysRevB.106.195203](https://doi.org/10.1103/PhysRevB.106.195203)**I. INTRODUCTION**

Re combines with the p elements of groups 13–14 yielding intermetallic compounds with interesting transport properties. Here, Al- and Ga-based ReGa_5 [1], ReAl_6 [2], and $\text{ReAl}_{1.2}\text{Si}_{0.8}$ [3], show superconducting properties at low temperatures. At the same time, Si- and Ge-containing ReGaSi [4], ReGaGe_2 [5], and ReGa_2Ge [6], exhibit narrow-gap semiconducting behavior. Finally, $\text{Re}_2\text{Ga}_9\text{Ge}$ demonstrates structural instability below room temperature [7], while for Re_3Ge_7 a metal–insulator-like electronic phase transition was reported [8]. Furthermore, the Ga for Ge substitution in Re_3Ge_7 gradually suppresses transition to the semiconducting state and induces superconductivity, which exhibits a dome-like behavior at low temperatures. The reported phase diagram points at the competition between semiconducting and superconducting states in $\text{Re}_3\text{Ge}_{7-x}\text{Ga}_x$ driven by the Fermi-surface nesting and nontrivial band topology [9]. A similar scenario, namely the competing superconductivity and structural stability, was recently proposed for endohedral cluster superconductors [1,10], which are the family of intermetallic compounds built by clusters of p metal atoms with the embedded transition metals.

According to this scenario, the Fermi levels of endohedral cluster superconductors, such as ReGa_5 [1], RuAl_6 [11], and PdGa_5 [12], are located in deep pseudogaps, an important fact that determines the chemical stability of such compounds [1]. The reduced density of states at the Fermi level eliminates a

destabilizing effect of the kinetic energy of valence electrons, and thus leads to an overall stability of the system. At the same time, a high density of states at the Fermi level is needed to achieve high critical temperatures of superconductivity, which naturally competes with structural stability. Interestingly, the appearance of pseudogaps and true band gaps in the electronic structures was explained in terms of the valence electron counting rules for a number of intermetallic structure types [13–18]. For example, the $18 - n$ rule formulated for the intermetallic compounds of transition metals and p metals, where n is the number of chemical bonds between transition-metal atoms, defines the optimum number of valence electrons, for which the Fermi level is located in a band gap or deep pseudogap [17]. Although many systems demonstrate slight deviations from the predicted valence electron count (VEC), intermetallic semiconductors, such as RuGa_2 [19], RuGa_3 [20], ReGa_3Zn [21], ReGa_2Ge [6], and ReGaGe_2 [5], exactly obey the $18 - n$ rule. In Re_3Ge_7 , which follows the generalized $18 - n + m$ rule [17], the semiconducting ground state emerges below the temperature of the metal–insulator electronic phase transition $T_{\text{MI}} = 58.5$ K [8]. Furthermore, the $\text{Re}_3\text{Ge}_{7-x}\text{Ga}_x$ solid solution demonstrates competing semiconducting and superconducting states. For $x = 0.2$, T_{MI} is reduced down to 47.7 K, while the superconductivity emerges below the critical temperature of $T_c = 1.81$ K. With increasing x , T_c exhibits a dome-like behavior with the maximum value of 3.37 K for $x = 0.25$. The unique electronic properties of Re_3Ge_7 build a bridge between the intermetallic semiconductors and endohedral cluster superconductors. From one hand, the compound follows simple electron counting rules and shows proximity to the semiconducting ground state. From the other hand, the hole doping induces bulk superconductivity

*valeriy.verchenko@gmail.com

accompanied by the nontrivial band topology in the electronic structure [9].

In this study, we probe the metal–insulator electronic phase transition in Re_3Ge_7 by temperature-dependent resistivity, thermopower, and high-resolution powder x-ray diffraction measurements. The experimental crystal structure parameters at the lowest measured temperature were used for comprehensive electronic structure calculations, which explain a possible origin of the metal–insulator transition.

II. EXPERIMENTAL DETAILS

Polycrystalline Re_3Ge_7 was prepared using the stoichiometric mixture of Re (powder, 99.995%, Sigma-Aldrich) and Ge (chips, 99.999%, Sigma-Aldrich). The starting materials with a total mass of 1 g were placed in an alumina crucible inside a quartz ampule, which was evacuated to the residual pressure of 5×10^{-3} mbar and flame-sealed. The ampule was annealed in a programmable furnace at 1273 K for 24 h and cooled to room temperature. The sample was ground in an agate mortar, enclosed inside an evacuated and sealed ampule, and annealed at 1073 K for 48 h. Crystal growth of Re_3Ge_7 was performed using the flux of Ge. Re and Ge were weighed in the molar ratio of 1:16 with a total mass of 1 g and placed inside a quartz ampule, which was evacuated and flame-sealed. The mixture was annealed at 1323 K for 48 h to obtain a homogenous melt, and slowly cooled to 1173 K at the rate of 1 K/h. The excess of Ge was removed by chemical vapor transport. For this, the obtained ingot was placed together with several crystals of iodine inside a quartz ampule, which was evacuated and flame-sealed. The concentration of I_2 of 1.4 mg/ml corresponds to an ampule with 130-mm length and 8-mm inner diameter. The ampule was placed inside a horizontal two-zone programmable furnace and annealed in the temperature gradient of 723–603 K for ten days. As a result, the excess of Ge was transferred to the cold zone, while high-quality needle-like single crystals of Re_3Ge_7 were found in the hot zone.

Single crystals were examined on a scanning electron microscope (SEM) JSM JEOL6490-LV equipped with an energy-dispersive x-ray (EDX) detection system INCA x-Sight. Figure 1 shows an optical image of the as-grown crystal with the evenly distributed Re and Ge species, according to EDX spectroscopy. Powder x-ray diffraction patterns of polycrystalline samples and crushed single crystals were collected on a Huber G670 Guinier camera [Cu x-ray source, Ge monochromator, $\lambda = 1.5406$ Å]. JANA2006 program was used for structure refinements by the Rietveld method [22].

Polycrystalline Re_3Ge_7 was studied employing high-resolution powder x-ray diffraction (HRPXR) at the ID22 beamline [$\lambda = 0.354178(2)$ Å, $2\theta_{\text{max}} = 41^\circ$] of the European Synchrotron Radiation Facility (ESRF, Grenoble, France) [23]. The data were collected by nine Si [111] analyzer crystals and an EIGER detector (EIGER2 X CdTe 2M-W) [24]. Measurements were conducted on the sample enclosed in a quartz capillary (0.4-mm diameter) purged with He gas and mounted inside a liquid He cooled cryostat. The data were collected at temperatures between 10 K and 100 K with a step of 10 K, and between 100 K and 300 K with a step of 20 K. Crystal structure refinements were performed in the JANA2006

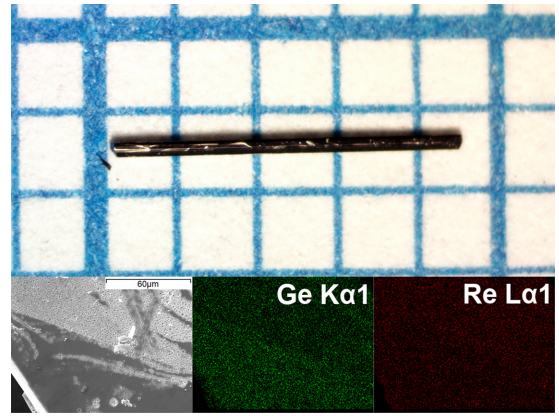


FIG. 1. Top: optical image of the Re_3Ge_7 single crystal. Bottom: SEM image of the crystal surface and distribution of the Re and Ge elements.

program [22] using the reported structural parameters of Re_3Ge_7 as a starting model [25]. The absorption correction was calculated assuming a cylindrical sample. Details of data collection and refinement are given in Table I. Parameters of atomic positions are listed in Table II. Temperature-dependent atomic displacement parameters were analyzed within the Debye approximation as implemented in the DEBYEFIT program [26].

TABLE I. Data collection and structure refinement parameters for Re_3Ge_7 .

Parameter	Value	
Composition	Re_3Ge_7	
M_w (g mol ⁻¹)	1067.031	
Diffractometer	ID22, ESRF	
Detector	9 Si (111) analyzer crystals, EIGER	
Radiation	Synchrotron	
Wavelength (Å)	0.354178(2)	
Scan mode	Debye-Scherrer	
Temperature (K)	300 K	10 K
Crystal system	Orthorhombic	
Space group	$Cmcm$	
Cell parameters (Å)	$a = 3.230964(6)$, $b = 9.05546(2)$ $c = 21.98890(4)$	$a = 3.225271(8)$, $b = 9.03391(2)$ $c = 21.92109(6)$
Cell volume (Å ³)	643.348(2)	638.711(3)
Z	4	
ρ_{calc} (g cm ⁻³)	11.01	11.09
μ (mm ⁻¹)	13.72	13.82
θ range (deg)	1.6–41	
No. of parameters	55	39
R_p	0.056	0.072
R_{wp}	0.079	0.099
$R_{\text{obs}}/wR_{\text{obs}}$	0.021/0.029	0.022/0.030
$R_{\text{all}}/wR_{\text{all}}$	0.021/0.028	0.023/0.032
Goodness-of-fit	2.91	4.38
Residual peaks (e Å ⁻³)	2.62/–2.74	3.39/–5.43

TABLE II. Atomic coordinates and displacement parameters for Re_3Ge_7 . The room-temperature and 10 K values are shown as regular and italic text, respectively.

Atom	Site	x	y	z	U_{eq} or U_{iso} (\AA^2)
Re1	8 <i>f</i>	0	0.07338(4)	0.55920(2)	0.0062(1)
		0	<i>0.07348(5)</i>	<i>0.55930(2)</i>	<i>0.00378(9)</i>
Re2	4 <i>c</i>	0	0.48181(6)	0.25	0.0063(2)
		0	<i>0.48175(7)</i>	<i>0.25</i>	<i>0.0035(1)</i>
Ge1	8 <i>f</i>	0	0.0596(1)	0.16220(4)	0.0088(3)
		0	<i>0.0605(1)</i>	<i>0.16222(5)</i>	<i>0.0047(2)</i>
Ge2	8 <i>f</i>	0	0.3239(1)	0.13637(4)	0.0090(3)
		0	<i>0.3247(1)</i>	<i>0.13648(5)</i>	<i>0.0047(2)</i>
Ge3	8 <i>f</i>	0	0.3534(1)	0.53250(4)	0.0073(3)
		0	<i>0.3535(1)</i>	<i>0.53232(5)</i>	<i>0.0042(2)</i>
Ge4	4 <i>c</i>	0	0.7638(2)	0.25	0.0096(4)
		0	<i>0.7640(2)</i>	<i>0.25</i>	<i>0.0048(3)</i>

Electronic structure calculations were performed within the density functional theory approach using the full-potential code FPLO (version 14-00.47) [27]. In the scalar relativistic regime, the general gradient approximation (GGA) was used to treat the exchange and correlation energy [28]. Integrations were performed by the improved tetrahedron method [29] on a grid of $12 \times 12 \times 16$ k -points in the first Brillouin zone. Electronic structure including spin-orbit coupling was calculated in the full-relativistic regime using a $8 \times 8 \times 12$ k -mesh.

Heat capacity was measured employing a relaxation-type calorimeter of the heat capacity option of a physical property measurement system (PPMS, Quantum Design) on a pelletized sample. The long-pulse technique was employed [30], according to which heat pulses of 30% temperature rise and 3τ measurement time were used, where τ is the first-order relaxation time constant. Measurements were performed by raising the temperature from 1.8 K to 100 K in a zero magnetic field. The dual-slope analysis of the heat capacity data was performed in a PPMS MULTIVU program (Quantum Design). Electrical resistance and the Seebeck coefficient were measured by the four-probe technique using the thermal transport option of PPMS (Quantum Design). Measurements were performed on a rectangular-shaped pellet with the dimensions of $8 \times 3 \times 2$ mm^3 , which was prepared by pressing polycrystalline Re_3Ge_7 at room temperature at an external pressure of 4 kbar. Transport properties were examined in the temperature range of 1.8–400 K in zero magnetic field.

III. RESULTS AND DISCUSSION

The room-temperature HRPXRD pattern of Re_3Ge_7 is shown in Fig. 2. Crystal structure refinement by the Rietveld method in the full-matrix anisotropic approximation confirms the reported structural model [25]. Re_3Ge_7 crystallizes in the $Cmcm$ space group and has no isostructural analogs. The related endohedral cluster compounds, ReGaGe_2 and ReGa_2Ge , respectively, crystallize in the MgCuAl_2 and IrIn_3 structure types and show similar coordination polyhedra [5,6]. In the listed compounds, Re atoms center two-capped and three-capped trigonal prisms of the p element atoms. Furthermore, the monoclinic crystal structure of the osmium germanide,

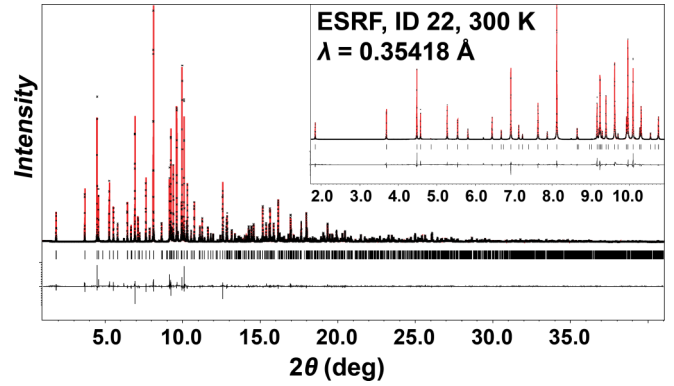


FIG. 2. Experimental (black dots) and calculated (red line) HRPXRD patterns of Re_3Ge_7 at room temperature. Positions of peaks are shown by black ticks and the difference curve is given by the black line in the bottom part.

OsGe_2 , shows a similar structural motif, where the columns of Os-centered trigonal prisms run along the $[010]$ direction. Remarkably, the related ReGaGe_2 and ReGa_2Ge endohedral cluster compounds are narrow-gap semiconductors [5,6]. Re_3Ge_7 exhibits a metal-insulator-like phase transition and shows proximity to the semiconducting ground state as well [8].

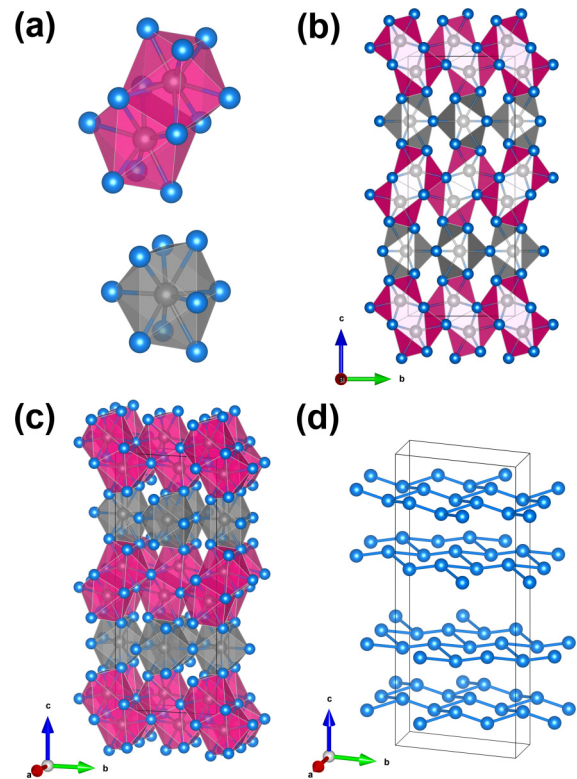


FIG. 3. Crystal structure of Re_3Ge_7 : (a) coordination polyhedra of the Re1 and Re2 atoms (pink and gray, respectively); (b) view along the $[100]$ direction; (c) polyhedral representation of the unit cell; and (d) corrugated layers of Ge atoms. Re atoms are shown in gray and Ge in blue.

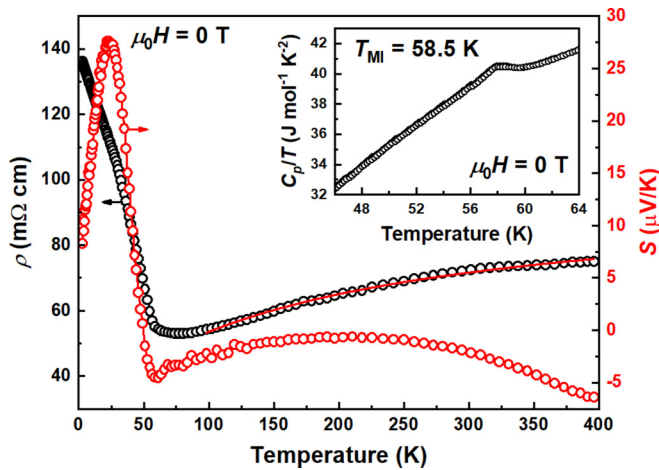


FIG. 4. Electrical resistivity (left axis) and Seebeck coefficient (right axis) of Re_3Ge_7 in zero magnetic field. The solid red line is a fit according to the parallel resistor model. The inset shows heat capacity in the vicinity of phase transition in zero magnetic field.

In the crystal structure of Re_3Ge_7 (Fig. 3), Re atoms occupy two crystallographic positions. The Re1 atoms center two-capped trigonal prisms of Ge atoms, Re1@Ge_8 . Two adjacent Re1@Ge_8 prisms have a common rectangular face, such that the Re–Re dumbbells are formed with the Re1–Re1 distance of 2.92 Å. The same structural unit can be found in the crystal structure of the ReGa_2Ge intermetallic semiconductor [6]. Taking into account the Re1–Re1 chemical bond, which is slightly larger than the Re–Re distance of 2.75 Å in metallic Re, the coordination polyhedron of Re1 can be viewed as a three-capped trigonal prism with two Ge and one Re making the caps. Similarly, the Re2 atoms are located inside three-capped trigonal prisms of Ge atoms, Re2@Ge_9 . Interestingly, the crystal structure of ReGaGe_2 is built by the isomorphous $\text{Re@}(\text{Ga}/\text{Ge})_9$ three-capped trigonal prisms [5]. The Re1- and Re2-based trigonal prisms form infinite columns along the [100] direction by sharing the triangular faces, and combine into layers, which alternate along the [001] direction [Fig. 3(b)]. The columns and layers are connected with each other by edges and vertices, building the entire three-dimensional framework of Re_3Ge_7 [Fig. 3(c)]. Remarkably, the Ge1 and Ge2 atoms connected by the short distances of 2.46 Å and 2.74 Å form corrugated nets of hexagons in the chair conformation perpendicular to the [001] direction [Fig. 3(d)]. These nets of Ge atoms are located exactly between the layers of Re1- and Re2-based trigonal prisms.

Figure 4 shows electrical resistivity and Seebeck coefficient of Re_3Ge_7 in zero magnetic field. The compound exhibits a metal–insulator electronic phase transition with no thermal hysteresis of transport properties in agreement with the previous reports [8,9]. The transition is clearly visible on the heat capacity curve as a λ -like anomaly at the characteristic temperature of $T_{\text{MI}} = 58.5$ K in zero magnetic field. Above the transition, electrical resistivity increases with increasing temperature indicating the metallic behavior. Low and negative values of the Seebeck coefficient typical for metals are observed in this temperature range. However, the increase of resistivity is gradual with a pronounced saturation

behavior at the elevated temperatures. Saturation of resistivity is observed in many metallic systems with large resistivities, for example, in the $\text{Mo}_8\text{Ga}_{41}$ and $\text{Mo}_6\text{Ga}_{31}$ endohedral cluster superconductors [31,32]. It occurs when the mean free path of charge carriers is comparable to interatomic distances according to the Ioffe-Regel condition [33]. The resistivity of Re_3Ge_7 above 100 K can be fitted using the parallel resistor formula $\rho(T)^{-1} = \rho_{\text{ideal}}(T)^{-1} + \rho_{\text{sat}}^{-1}$, where ρ_{sat} is a saturation resistivity and $\rho_{\text{ideal}}(T)$ is the Boltzmann-type resistivity, which is linear in T at the elevated temperatures (Fig. 4). Fitting the resistivity data yields $\rho_{\text{sat}} = 96(2)$ mΩ cm well above the Ioffe-Regel resistivity [33] and the linear slope of $0.020(4)$ Ω m K⁻¹, which is comparable to that of the RuAl_6 and Rh_2Ga_9 endohedral cluster superconductors [11,34]. The actual mechanism of resistivity saturation is strongly debated in the literature. It may be due to electron-phonon or electron-electron scattering [33,35–37]. Also, the peculiarities of the band structure [38] or weak localization of conduction electrons may play an important role [39,40]. Moreover, statistical analysis of various saturating systems reveals that there is no universal analytical expression explaining the saturation behavior [41]. In Re_3Ge_7 , which shows good crystallinity according to the HRPXRD data (Fig. 2), the scattering on structural defects can be excluded. Furthermore, the proximity to the semiconducting ground state as well as the observed low density of states at the Fermi level (see below) suggest that electron-electron interactions are not present in Re_3Ge_7 . Thus, peculiar electron-phonon coupling should be taken into account as a possible reason of the saturating resistivity.

Below the transition, ρ sharply increases, while S changes its sign and exhibits a maximum located at 24 K. The maximum value of S , which is 27 $\mu\text{V}/\text{K}$, shows an enhancement in comparison with the values typical for metals. The peak of the Seebeck coefficient is a remarkable feature of the low-temperature semiconductor-like state. Interestingly, intermetallic compounds with the semiconducting properties may exhibit a large peak of the Seebeck coefficient at low temperatures. For example, narrow-gap semiconductors CrSb_2 [42], FeSb_2 [43], and FeGa_3 [44] demonstrate S as low as -4500 $\mu\text{V}/\text{K}$, $-45\,000$ $\mu\text{V}/\text{K}$, and $-16\,000$ $\mu\text{V}/\text{K}$ below 20 K, respectively. In this list, FeSb_2 exhibits a metal–semiconductor crossover, when the current is applied along the b axis, at temperatures between 40 K and 80 K depending on the current alignment [45]. Possible reasons of the unexpected peak of S include the presence of strong electronic correlations; structural, magnetic, or electronic phase transitions; and interaction of phonons with charge carriers via phonon-drag effect. The last item is likely present in the colossal thermopower materials CrSb_2 [42], FeGa_3 [44], and FeSb_2 [46]. On the one hand, Re_3Ge_7 does not show signatures of the strong correlation effects. [8,9]. On the other hand, its transport properties are similar to those of FeSb_2 and oxygen-deficient TiO_2 [47], which demonstrate metal–semiconductor transition in the midtemperature range and nontrivial thermoelectric properties at low temperatures. Presumably, the phonon-drag effect may be present in the low-temperature semiconductor-like state of Re_3Ge_7 that fosters its further investigation.

The electronic phase transition of Re_3Ge_7 was probed by HRPXRD measurements. The HRPXRD patterns

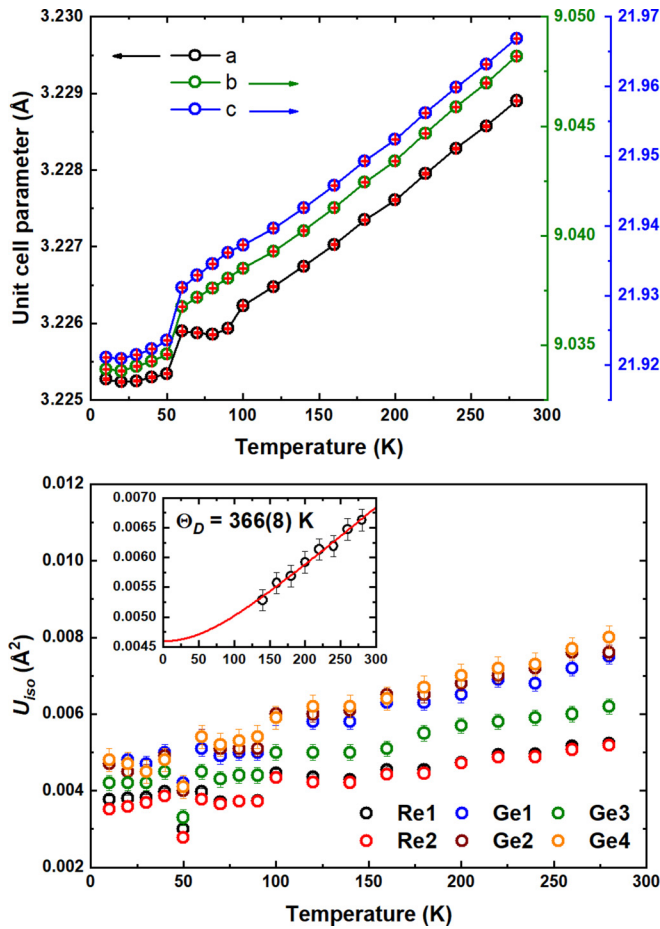


FIG. 5. Top: Unit cell parameters of Re_3Ge_7 as a function of temperature. Bottom: Temperature-dependent atomic displacement parameters. The inset shows atomic displacement parameter averaged over all crystallographic sites. The solid red line is a fit according to the Debye model.

collected below the transition temperature of $T_{\text{MI}} = 58.5$ K show no additional superstructure reflections. Furthermore, crystal structure refinements can be performed using the room-temperature structural model in the entire temperature range studied. Tables I and II show refinement details and atomic position parameters for the crystal structure of Re_3Ge_7 at the lowest measured temperature of 10 K. Figure 5 shows the refined unit cell parameters of Re_3Ge_7 as a function of temperature. The unit cell volume decreases with decreasing temperature. In the vicinity of the transition temperature a , b , and c parameters of the orthorhombic unit cell, as well as the unit cell volume, show a sharp kink, which is characteristic of a second-order phase transition. At the same time, the Re1–Re1 and Ge1–Ge2 interatomic distances, as well as the average Re–Ge distances in the first coordination sphere of Re1 and Re2 atoms are weakly temperature-dependent (Fig. 6). Accordingly, the principal coordination polyhedra do not show sharp contraction in the vicinity of phase transition and the shrinkage of the unit cell volume is due to interatomic changes taking place in the second coordination sphere. In the previous report, a temperature-dependent powder x-ray diffraction study did not

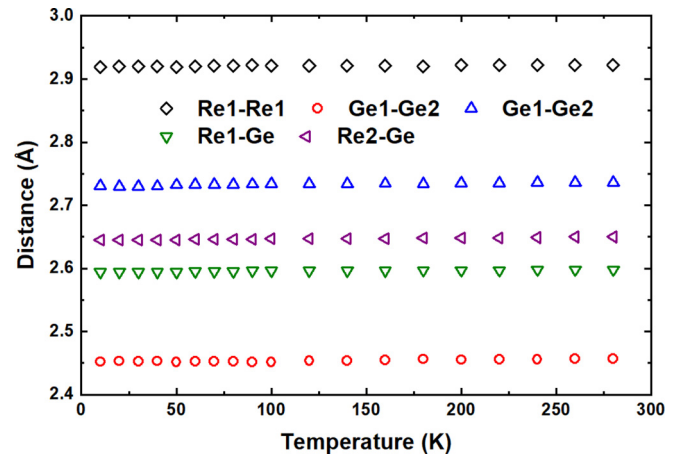


FIG. 6. Main interatomic distances in the crystal structure of Re_3Ge_7 as a function of temperature. The Re1–Ge (green triangles) and Re2–Ge (violet triangles) are averaged distances in the first coordination environment of the Re1 and Re2 atoms, respectively.

reveal any anomaly in the vicinity of transition, presumably due to the poor temperature control of the experiment [9].

Temperature evolution of atomic displacement parameters (ADP) is shown in Fig. 5, bottom panel. All crystallographic sites display gradual increase of ADPs with increasing temperature. The noticeable dip located at 50 K below T_{MI} indicates a slight contraction of the electronic density right below the metal–insulator transition. At temperatures above 140 K, all ADPs are linear in T in agreement with the Debye model. The average atomic displacement parameter, which is shown in the inset of Fig. 5, was calculated taking into account the multiplicities of the crystallographic sites. The fitting yields the Debye temperature of $\Theta_D = 366(8)$ K, which is in reasonable agreement with the value derived from the heat capacity data [9].

Crystal structure parameters of Re_3Ge_7 obtained at 10 K (Tables I and II) were used for electronic structure calculations. The calculated density of states (DOS), which is shown in Fig. 7, contains three pockets of states separated by the pseudogaps located at -6.5 eV and -0.5 eV. The electronic structure between -14 eV and -6.5 eV is primarily composed of the bonding Ge $4s$ states. At higher energies, strong mixing of the Re $5d$ and Ge $4p$ states occurs yielding a peak structure of the DOS. Similar features of the electronic structure were observed in various endohedral cluster superconductors, where the d states of a transition-metal atom, which centers the endohedral cluster, strongly hybridize with the p states of main-group metal located in the vertices [1,11,31,32,48–50]. Including spin-orbit coupling induces band splitting mainly on top of the valence band along the Y - Z and Z - T directions. As a result, the main gap located at -0.5 eV collapses yielding nontrivial half-metallic features of the electronic structure in this energy region.

As a result of strong d - p hybridization, a pseudogap may appear near the Fermi level separating the bonding and antibonding states. The valence electron count, which corresponds to the position of a pseudogap, defines the optimum filling of bands in the electronic structure, where all bonding states are occupied and antibonding states are vacant. The

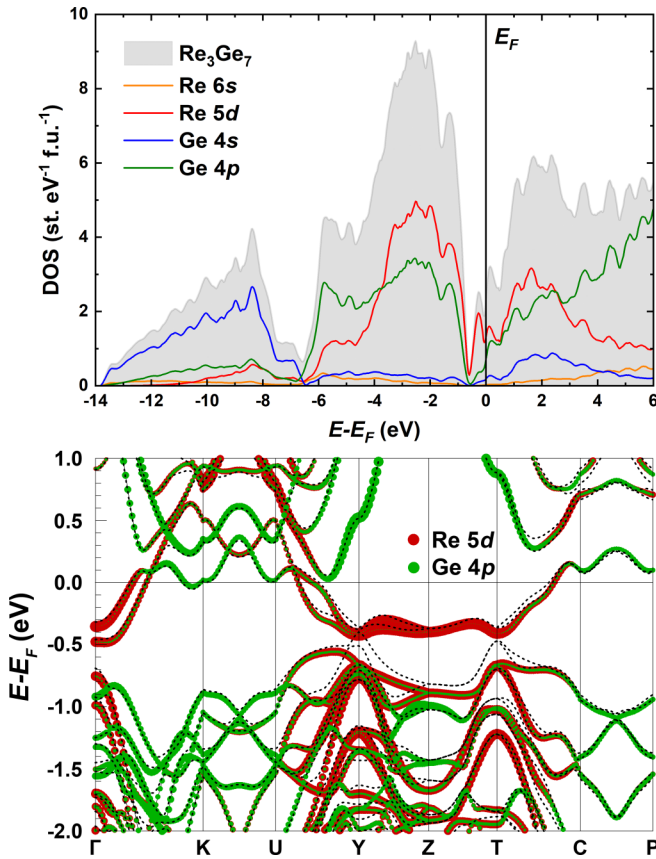


FIG. 7. Calculated density of states (top panel) and band structure (bottom panel) of Re_3Ge_7 . The band-structure-including spin-orbit coupling is shown by the black dashed line.

concept of valence electron count was employed to predict the compositional and stability ranges of various intermetallic structure types [17,51]. However, the situation may be hindered due to the formation of several pseudogaps close to each other. Furthermore, partial filling of the antibonding states can be observed, which not always competes with the thermodynamic stability [48,52].

In Re_3Ge_7 , the main pseudogap is located at the relative energy of -0.5 eV and corresponds to the $\text{VEC} = 16 e^-$ per Re atom. However, for the Re_3Ge_7 stoichiometric composition, which has $\text{VEC} = 16.33 e^-$ per Re atom, the Fermi level is located in the second pseudogap between two peaks of DOS. In the electronic structure, only two crystal bands with the Re 5d and Ge 4p contributions cross the Fermi level. The observed DOS at the Fermi level is $N(E_F) = 1.9$ st. $e\text{V}^{-1}$ f.u. $^{-1}$. This feature of the electronic structure may be at the origin of the observed electronic phase transition. Indeed, the calculated electronic structure corresponds to the metallic ground state, which is observed above $T_{\text{MI}} = 58.5$ K. The transition to the semiconducting state may be accompanied

by the opening of a band gap at E_F and transformation of low DOS near the Fermi level into the in-gap states. The presence of in-gap states in the vicinity of E_F was documented for the FeGa_3 and FeSb_2 intermetallic semiconductors [53], which exhibit colossal values of thermopower at low temperatures [43,44].

IV. CONCLUSION

Re_3Ge_7 endohedral cluster compound is a unique electronic material, where the low-temperature semiconducting state, which emerges as a result of the metal–insulator phase transition, is found close to the dome-like superconducting phase induced by hole doping. The structural motif of the compound has similarities with both semiconducting and superconducting endohedral cluster frameworks. In the crystal structure of Re_3Ge_7 , Re atoms are embedded in two-capped and three-capped trigonal prisms of Ge atoms. The same endohedral clusters with the mixed Ge/Ga atoms build the crystal structures of ReGa_2Ge and ReGaGe_2 intermetallic semiconductors, while the Ga-based $\text{Re}@Ga_9$ clusters are the building units of superconducting ReGa_5 . Mixing of Ga/Ge atoms in the crystal structure is a tool to control the valence electron count that determines the ground-state properties of the listed electronic phases, including Re_3Ge_7 .

In Re_3Ge_7 , electrical resistivity and Seebeck coefficient measurements indicate substantial changes of the electronic structure during the metal–insulator phase transition. Furthermore, both the saturation of resistivity at high temperatures and unexpected peak of the Seebeck coefficient in the semiconductor-like state at low temperatures point at the peculiar electron-phonon coupling. The electronic structure calculations reveal two deep pseudogaps located at the valence electron count of 16 and $16.33 e^-$ per Re atom, with the Fermi level located in the second one. The Ga for Ge substitution, reported recently, reduces the VEC and shifts the Fermi level toward the main pseudogap. At the same time, the bulk superconductivity is induced in the system. Given the second-order nature of phase transition in Re_3Ge_7 unveiled by the temperature-dependent structural studies, we conclude that the valence electron count and fine electronic structure in the vicinity of the Fermi energy are two main factors that determine the electronic properties of Re_3Ge_7 .

ACKNOWLEDGMENTS

This work is partially supported by the Ministry of Science and Higher Education of Russian Federation, Grant No. 075-15-2021-1353. V.Y.V. is grateful for the financial support provided by the European Regional Development Fund and the program Mobilitas Plus (Grant No. MOBJD449). The authors acknowledge the European Synchrotron Radiation Facility for granting the beam time for experiment HC-4105 and thank Dr. Ola G. Grendal for her help during the high-resolution PXR experiments.

[1] W. Xie, H. Luo, B. F. Phelan, T. Klimczuk, F. A. Cevallos, and R. J. Cava, *Proc. Natl. Acad. Sci.* **112**, E7048 (2015).

[2] D. C. Peets, E. Cheng, T. Ying, M. Kriener, X. Shen, S. Li, and D. Feng, *Phys. Rev. B* **99**, 144519 (2019).

- [3] V. Decocq, X. Gui, A. Neeson, W. Xie, T. Heitmann, and F. Wang, *Inorg. Chem.* **59**, 17310 (2020).
- [4] W. Xie, L. Gustin, and G. Bian, *Inorg. Chem.* **56**, 5165 (2017).
- [5] M. S. Likhanov, R. A. Khalaniya, V. Y. Verchenko, A. A. Gippius, S. V. Zhurenko, A. V. Tkachev, D. I. Fazlizhanova, A. N. Kuznetsov, and A. V. Shevelkov, *Chem. Commun.* **55**, 5821 (2019).
- [6] M. S. Likhanov, V. Y. Verchenko, A. A. Gippius, S. V. Zhurenko, A. V. Tkachev, Z. Wei, E. V. Dikarev, A. N. Kuznetsov, and A. V. Shevelkov, *Inorg. Chem.* **59**, 12748 (2020).
- [7] M. S. Likhanov, V. Y. Verchenko, V. O. Zhupanov, Z. Wei, E. V. Dikarev, A. N. Kuznetsov, and A. V. Shevelkov, *Inorg. Chem.* **61**, 568 (2022).
- [8] A. Rabus and E. Mun, *Phys. Rev. Mater.* **3**, 013404 (2019).
- [9] Y. Cui, S. Wu, Q. Zhu, G. Xiao, B. Liu, J. Wu, G. Cao, and Z. Ren, *npj Quantum Mater.* **6**, 74 (2021).
- [10] V. Y. Verchenko and A. V. Shevelkov, *Dalton Trans.* **50**, 5109 (2021).
- [11] Z. Ryżyńska, J. R. Chamorro, T. M. McQueen, P. Winiewski, D. Kaczorowski, W. Xie, R. J. Cava, T. Klimczuk, and M. J. Winarski, *Chem. Mater.* **32**, 3805 (2020).
- [12] Z. Ryżyńska, P. Winiewski, D. Kaczorowski, W. Xie, R. J. Cava, T. Klimczuk, and M. J. Winarski, *J. Phys. Chem. C* **125**, 11294 (2021).
- [13] D. Bende, F. R. Wagner, and Y. Grin, *Inorg. Chem.* **54**, 3970 (2015).
- [14] D. C. Fredrickson, S. Lee, and R. Hoffmann, *Inorg. Chem.* **43**, 6159 (2004).
- [15] V. J. Yannello, B. J. Kilduff, and D. C. Fredrickson, *Inorg. Chem.* **53**, 2730 (2014).
- [16] R. T. Fredrickson and D. C. Fredrickson, *Inorg. Chem.* **51**, 10341 (2012).
- [17] V. J. Yannello and D. C. Fredrickson, *Inorg. Chem.* **54**, 11385 (2015).
- [18] V. J. Yannello and D. C. Fredrickson, *Inorg. Chem.* **53**, 10627 (2014).
- [19] J. Evers, G. Oehlinger, and H. Meyer, *Mater. Res. Bull.* **19**, 1177 (1984).
- [20] U. Häussermann, M. Boström, P. Viklund, Ö. Rapp, and T. Björnängen, *J. Solid State Chem* **165**, 94 (2002).
- [21] V. Y. Verchenko, A. V. Mironov, Z. Wei, A. A. Tsirlin, E. V. Dikarev, and A. V. Shevelkov, *Inorg. Chem.* **58**, 1561 (2019).
- [22] V. Petříček, M. Dušek, and L. Palatinus, *Z. Kristallogr. - Cryst. Mater.* **229**, 345 (2014).
- [23] V. Y. Verchenko and O. Grendal, Metal-to-insulator electronic phase transition in the Re_3Ge_7 endohedral cluster compound, European Synchrotron Radiation Facility, <https://doi.org/10.1515/ESRF-ES-395241975?urlappend=%3Fref%3DPDF&javVoR&relcite-as>, 2024.
- [24] C. Dejoie, M. Coduri, S. Petitdemange, C. Giacobbe, E. Covacci, O. Grimaldi, P.-O. Autran, M. W. Mogodi, D. Šišák Jung, and A. N. Fitch, *J. Appl. Crystallogr.* **51**, 1721 (2018).
- [25] T. Siegrist, F. Hulliger, and W. Petter, *J. Less-Common Met* **90**, 143 (1983).
- [26] A. P. Dudka, N. B. Bolotina, and O. N. Khrykina, *J. Appl. Crystallogr.* **52**, 690 (2019).
- [27] K. Koepnick and H. Eschrig, *Phys. Rev. B* **59**, 1743 (1999).
- [28] J. P. Perdew, K. Burke, and M. Ernzerhof, *Phys. Rev. Lett.* **77**, 3865 (1996).
- [29] P. E. Blöchl, O. Jepsen, and O. K. Andersen, *Phys. Rev. B* **49**, 16223 (1994).
- [30] A. Scheie, *J. Low Temp. Phys.* **193**, 60 (2018).
- [31] V. Y. Verchenko, A. A. Tsirlin, A. O. Zubtsovskiy, and A. V. Shevelkov, *Phys. Rev. B* **93**, 064501 (2016).
- [32] V. Y. Verchenko, A. O. Zubtsovskii, A. A. Tsirlin, Z. Wei, M. Roslova, E. V. Dikarev, and A. V. Shevelkov, *J. Alloys Compd* **848**, 156400 (2020).
- [33] O. Gunnarsson, M. Calandra, and J. E. Han, *Rev. Mod. Phys.* **75**, 1085 (2003).
- [34] T. ShibaYama, M. Nohara, H. Aruga Katori, Y. Okamoto, Z. Hiroi, and H. Takagi, *J. Phys. Soc. Jpn.* **76**, 073708 (2007).
- [35] P. B. Allen, in *Superconductivity in D- and F-Band Metals*, edited by H. Suhl and M. B. Maple (Academic, New York, 1980), pp. 291–304.
- [36] P. Allen, *Inst. Phys. Conf. Ser. No.* **55**, 425 (1980).
- [37] I. L. Aleiner and O. Agam, *Ann. Phys. (NY)* **385**, 716 (2017).
- [38] J. K. Glasbrenner, B. S. Pujari, and K. D. Belashchenko, *Phys. Rev. B* **89**, 174408 (2014).
- [39] J. J. Lin and C. Y. Wu, *Phys. Rev. B* **48**, 5021 (1993).
- [40] B. Sundqvist, *Phys. Lett. A* **400**, 127291 (2021).
- [41] B. Sundqvist, *J. Phys. Chem. Solids* **165**, 110686 (2022).
- [42] B. C. Sales, A. F. May, M. A. McGuire, M. B. Stone, D. J. Singh, and D. Mandrus, *Phys. Rev. B* **86**, 235136 (2012).
- [43] A. Bentien, S. Johnsen, G. K. H. Madsen, B. B. Iversen, and F. Steglich, *Europhys. Lett.* **80**, 17008 (2007).
- [44] M. Wagner-Reetz, D. Kasinathan, W. Schnelle, R. Cardoso-Gil, H. Rosner, Y. Grin, and P. Gille, *Phys. Rev. B* **90**, 195206 (2014).
- [45] C. Petrovic, J. W. Kim, S. L. Bud'ko, A. I. Goldman, P. C. Canfield, W. Choe, and G. J. Miller, *Phys. Rev. B* **67**, 155205 (2003).
- [46] M. Battiato, J. M. Tomczak, Z. Zhong, and K. Held, *Phys. Rev. Lett.* **114**, 236603 (2015).
- [47] J. Tang, W. Wang, G.-L. Zhao, and Q. Li, *J. Phys.: Condens. Matter* **21**, 205703 (2009).
- [48] V. Y. Verchenko, A. A. Tsirlin, and A. V. Shevelkov, *Inorg. Chem. Front.* **8**, 1702 (2021).
- [49] V. Y. Verchenko, A. O. Zubtsovskii, Z. Wei, A. A. Tsirlin, E. V. Dikarev, and A. V. Shevelkov, *Dalton Trans.* **48**, 7853 (2019).
- [50] V. Y. Verchenko, A. O. Zubtsovskii, Z. Wei, A. A. Tsirlin, M. Marcin, A. V. Sobolev, I. A. Presniakov, E. V. Dikarev, and A. V. Shevelkov, *Inorg. Chem.* **58**, 15552 (2019).
- [51] D. C. Fredrickson, *Acc. Chem. Res.* **51**, 248 (2018).
- [52] V. Y. Verchenko and A. A. Tsirlin, *Inorg. Chem.* **61**, 3274 (2022).
- [53] A. A. Gippius, V. Y. Verchenko, A. V. Tkachev, N. E. Gervits, C. S. Lue, A. A. Tsirlin, N. Büttgen, W. Krätschmer, M. Baenitz, M. Shatruk, and A. V. Shevelkov, *Phys. Rev. B* **89**, 104426 (2014).